

A Unified Generation-Registration Framework for Improved MR-based CT Synthesis in Proton Therapy

Xia Li^{1,2}, Renato Bellotti^{1,3}, Barbara Bachtiary¹, Jan Hrbacek¹,
Damien C. Weber^{1,4,5}, Antony J. Lomax^{1,3}, Joachim M. Buhmann²,
Ye Zhang¹

1. Center for Proton Therapy, Paul Scherrer Institut, 5232 Villigen PSI

2. Department of Computer Science, ETH Zürich, 8092 Zürich

3. Department of Physics, ETH Zürich, 8092 Zürich

4. Department of Radiation Oncology, University Hospital of Zürich, 8091 Zürich

5. Department of Radiation Oncology, Inselspital, Bern University Hospital, University of Bern,
3010 Bern Version typeset January 24, 2024

Keywords: MR-to-CT synthesis, deformable registration, head-and-neck, proton therapy, implicit neural representation, nnUnet

Author to whom correspondence should be addressed. Email: ye.zhang@psi.ch

Abstract

Background: The use of Magnetic Resonance (MR) imaging for proton therapy treatment planning is gaining attention as a highly effective method for guidance. At the core of this approach is the generation of Computed Tomography (CT) images from MR scans. However, the critical issue in this process is accurately aligning the MR and CT images, a task that becomes particularly challenging in frequently moving body areas, such as the head-and-neck. Misalignments in these images can result in blurred synthetic CT (sCT) images, adversely affecting the precision and effectiveness of the treatment planning.

Purpose: This study introduces a novel network that cohesively unifies image generation and registration processes to enhance the quality and anatomical fidelity of sCTs derived from better-aligned MR images.

Methods: The approach synergizes a generation network (G) with a deformable registration network (R), optimizing them jointly in MR-to-CT synthesis. This goal is achieved by alternately minimizing the discrepancies between the generated/registered CT images and their corresponding reference CT counterparts. The generation network employs a UNet architecture, while the registration network leverages an implicit neural representation of the Deformable Vector Fields (DVF). We validated this method on a dataset comprising 60 Head-and-Neck patients, reserving 12 cases for holdout testing.

Results: Compared to the baseline Pix2Pix method with MAE 124.95 ± 30.74 HU, the proposed technique demonstrated 80.98 ± 7.55 HU. The unified translation-registration network produced sharper and more anatomically congruent outputs, showing superior efficacy

in converting MR images to sCTs. Additionally, from a dosimetric perspective, the plan recalculated on the resulting sCTs resulted in a remarkably reduced discrepancy to the reference proton plans.

Conclusions: This study conclusively demonstrates that a holistic MR-based CT synthesis approach, integrating both image-to-image translation and deformable registration, significantly improves the precision and quality of sCT generation, particularly for the challenging body area with varied anatomic changes between corresponding MR and CT.

Contents

I. Introduction	1
II. Methods	3
II.A. Generation Network	3
II.B. Deformable Registration Networks	5
II.C. Alternated Optimization	5
II.D. Dataset	6
II.E. Preprocessing	7
II.F. Image-level Evaluation	7
II.G. Dosimetric-level Evaluation	8
III. Results	8
III.A. Evaluation for sCT Generation	9
III.B. Alignment Evaluation	10
III.C. Dosimetric-level Evaluation	11
IV. Discussion	15
V. Conclusion	17
Acknowledgments	19
Appendix	19
References	20

I. Introduction

Proton therapy is distinguished by its precision and minimal radiation exposure to non-target tissues, necessitating accurate anatomical information for effective dose delivery¹. A critical aspect of this process requires the integration of Magnetic Resonance (MR) and Computed Tomography (CT) imaging². Although useful, due to the statistical global similarity metrics, cross-modality registration between MR and CT is often plagued by residual alignment issues, leading to inaccuracies in treatment planning. MR-based CT synthesis emerges as a pivotal solution in this context, particularly for Daily Adaptive Proton Therapy³ (DAPT), where reducing the daily radiation dose for imaging arises as a primary concern. By generating CT-like images from MR scans, this method bridges the gap between MR's superior soft tissue contrast and the essential electron density information provided by CT⁴. This approach not only offers the potential to bypass the misalignment issues⁵ inherent in conventional multi-modality registration methods but also reduces imaging radiation to patients⁶. The accuracy of these sCT images becomes especially crucial in proton therapy⁷, where even marginal inaccuracies can significantly alter the proton dose distribution, ultimately affecting the treatment outcome. This challenge is further amplified in anatomical regions subject to movement or deformation, such as the head-and-neck area⁸.

The integration of deep learning (DL) technologies in the synthesis of CT images from MR data represents a notable advancement in medical imaging^{9,10,11,12}. These DL methods utilize sophisticated neural networks, and adapt to complex feature recognition and learning, to effectively bridge the variations inherent between MR and CT imaging modalities¹³. Research has validated the efficacy of various MR and CT sequences in synthesizing CTs^{14,15,16,17,18}, particularly those proficient in delineating bone structures^{19,20} or from low-field images^{21,22}. Moreover, diverse training configurations and evaluation settings have been thoroughly investigated. These include different input dimensions^{22,23} (2D, 2.5D, 3D), input sizes^{22,24,25} (patch-wise, full size), and imaging planes^{24,26,27} (axial-only, three-planes). Additionally, several studies have focused on developing specialized network architectures for both generative^{28,29,30,31,32} and discriminative^{33,34} networks to enhance accuracy in CT generation, or compared the performance among different network structure designs^{35,36,37}. Innovative training losses^{38,39}, data standardization⁴⁰ and strategies^{41,42} have been devised to optimize model performance. Beyond image-level assessments, some approaches also integrate dosimetric-level evaluations, applicable in various thera-

peutic contexts like IMRT^{10,43}, VMAT⁴³, proton therapy^{44,45,45} and other modalities⁴⁶. There also exist some works that consider the practical problems such as data from multi-centers^{47,48}, the truncated MR⁴⁹, intestinal gas⁵⁰, MR-linac workflow⁵¹ and etc.

Despite significant advances thanks to DL technologies, a critical challenge in MR-based CT synthesis is the scarcity of paired and “ideal-aligned” training MR-CT pairs. The accuracy and quality of synthetic CT (sCT) images rely heavily on the quality of these data pairs^{5,52,53}, making it crucial for clinical application. While some works explored the CycleGAN architecture to enforce cycle consistency^{54,55,56,57} for this data-lacking issue, it tends to generate artifacts and is less accurate than Pix2Pix when roughly aligned paired data are available^{24,58,59}. The collection of such paired MR-CT images demands close temporal proximity between the scans of the same patient, significantly limiting the number of viable cases. Furthermore, achieving alignment is challenging due to the inherent differences in tissue representation between MRI and CT and sequential image acquisition by the two modalities. Often, solutions have tended to apply deformable image registration (DIR) between the planning CT and MR to minimize the unavoidable anatomic differences. However, only global metrics like mutual information (MI) can be used for similarity comparison, which may not sufficiently capture local image details, leading to suboptimal registration. Contemporary methods on deformable registration are shifting towards a dual approach^{60,61}: employing a generation network to map images to a uniform modality, followed by registration using more sensitive metrics such as mean absolute error (MAE). This approach highlights the interdependent nature of conditional image generation and cross-modality registration, creating a complex interplay akin to a chicken-and-egg scenario.

Our research proposes an innovative solution that jointly addresses these two challenges, introducing a groundbreaking framework that seamlessly integrates image generation and registration. This approach jointly optimizes the generation of synthetic CTs (sCTs) based on MR images and aligns these MR images with the planning CT. Contrary to prior methods that utilized generation to aid registration^{60,61}, our approach achieves the inverse effect, with deformable registration enhancing image generation quality. The registration component, constructed using the latest Implicit Neural Representation concept⁶², maps 3D coordinates and case identifiers to corresponding Displacement Vector Fields (DVFs), thereby encoding the deformations of training cases⁶³. This robust registration fitting significantly aids the generation network in training progressively more aligned MR-CT pairs, ensuring high anatomical fidelity in the synthesized images. This method is particularly advantageous in dynamic regions, where conventional DIR methods

are challenged due to misalignments in MRI and CT images. Consequently, the produced sCT images are more accurately value-mapped and anatomically precise, making them highly suitable for the stringent radiotherapy requirements, particularly for proton therapy planning.

Our approach was thoroughly evaluated at both the image and dosimetric levels, demonstrating high conformity of the synthetic CT to the input MR and significantly reducing voxel-wise errors. These robust experimental results substantiate two key assertions: 1) Joint registration significantly enhances the training of the generation network. The process of alternating optimization functions is similar to coordinate optimization, where both generation and registration errors are minimized in alternation. This alternation leads to progressively better alignment, allowing the generation network to concentrate predominantly on image intensity mapping rather than compensating for spatial deviations. 2) Joint registration also significantly improves the quality of the resulting synthetic CT images. Evaluations using imperfectly registered MR and CT images can be misleading, as errors can arise from both conditional image generation and the misalignment of the dataset. By facilitating better-aligned MR images that closely resemble actual CT scans, our proposed framework effectively minimizes errors attributable to spatial deviations, thus offering a more accurate assessment of synthetic CT quality.

II. Methods

II.A. Generation Network

The UNet architecture employed in our study serves as the backbone for the MR-to-CT image generation process G , as shown in Fig.1.a. This architecture is characterized by its symmetrical design, where the input MR images undergo a series of transformations through convolution, instance normalization, and max-pooling layers. These layers effectively compress the image into a condensed representation, capturing vital high-level features. Initially, the spatial dimensions of the image slice are mapped from 256×256 voxels to a compact feature map of $512 \times 16 \times 16$. Following this encoding pathway, the network transitions to a decoding phase. Here, deconvolution layers progressively restore the spatial dimensions, ultimately generating the sCT image. An essential aspect of the UNet architecture is implementing skip connections between corresponding encoding and decoding layers. These connections are crucial for retaining and incorporating intricate details from the MR images into the sCT output. For an in-depth understanding of

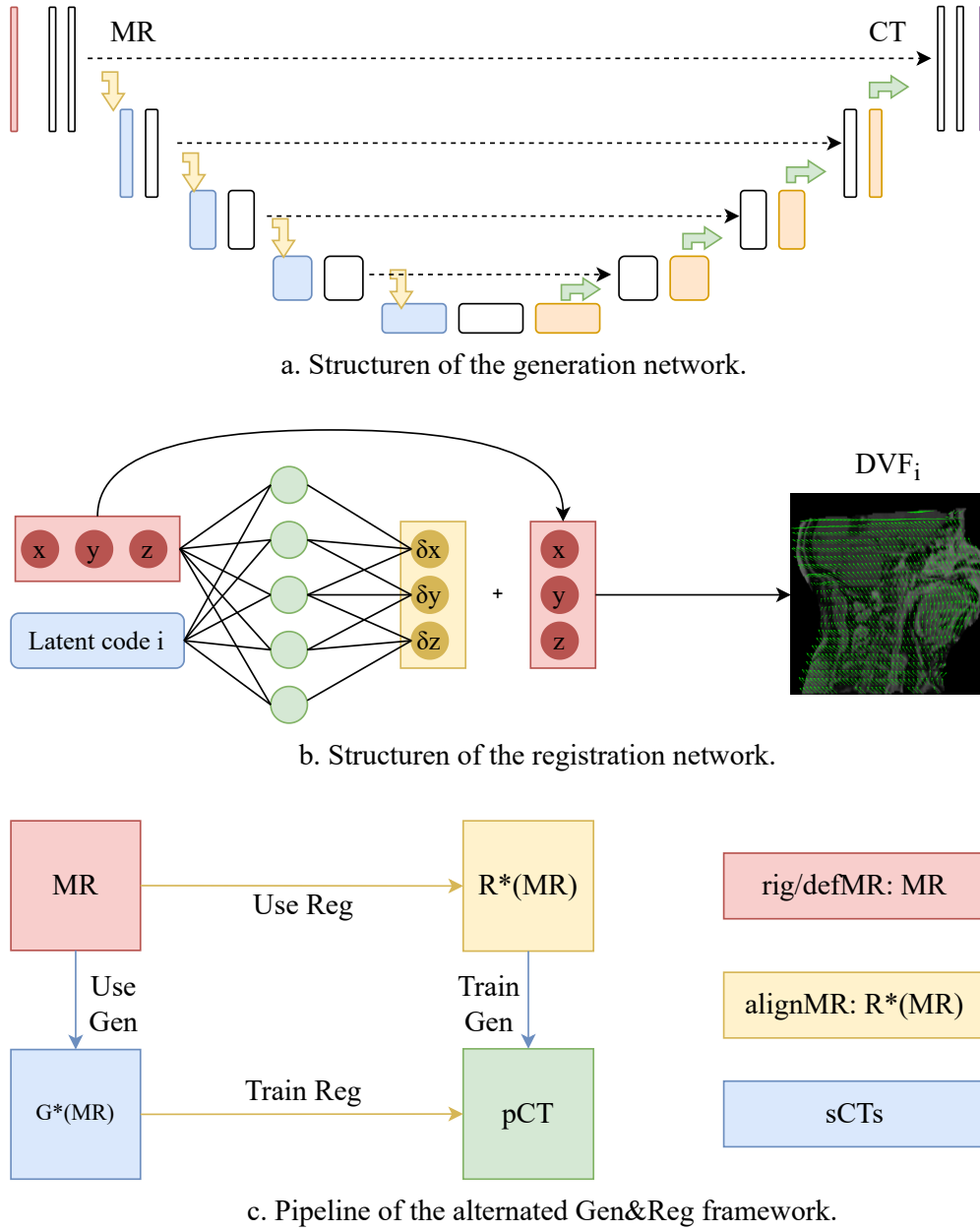


Figure 1: Structures of the networks and pipeline of the alternated framework.

the network's specific configurations and operational mechanisms, the readers are encouraged to consult the nn-UNet framework⁶⁴.

II.B. Deformable Registration Networks

In image registration, conventional methods have predominantly focused on networks that learn to predict DVFs using paired inputs like MR and planning CT (pCT)⁶⁵, or sCT and pCT⁶⁶. These networks, trained on either 2D slices⁶⁷ or low-resolution 3D images⁶⁸, have limitations, especially in achieving high-quality 3D deformable registration. They are trained to generalize on testing datasets, instead of fitting the registration of training images. Our method represents a departure from these conventional techniques. We have adopted an innovative approach to fit all DVFs for the training dataset. This strategy aligns more with our overarching goal of employing registration as an auxiliary tool in image generation. The implementation leverages the latest concept of Implicit Neural Representation (INR), an effective method for representing volumetric DVF's in continuous space⁶⁹ (IDIR). This technique maps the continuous input 3D coordinates $p_j = (x, y, x)$ of the j -th voxel to the corresponding displacement vectors $\delta p_j = (\delta x, \delta y, \delta z)$. Unlike the original IDIR⁶⁹, where each case fits into a separate network, we use a shared Multilayer Perceptron (MLP), as illustrated in Fig.1.b. Each case is identified by a unique learnable latent code c_i as in⁷⁰, streamlining the training process. This shared MLP model alleviates computational demands and considerably reduces memory and storage needs. The efficiency and scalability of our method are particularly beneficial when handling the large datasets commonly encountered in medical imaging.

II.C. Alternated Optimization

As depicted in Fig.1.c, our novel approach alternatively optimizes the generation (G) and registration (R) networks through an alternating process. The entire framework was trained for 100 epochs, with a 10-epoch cycle marking the switch between G and R. This cycle commenced with G's training using the registered MR, denoted as $R^*(MR)$ to the pCT, followed by the generation of the sCT, represented as $G^*(MR)$ with the freshly trained G from the last iteration. Subsequently, R was trained using sCT as $G^*(MR)$ alongside the pCT. After this, DVFs inferred from R were applied to warp the MR into $R^*(MR)$, setting the stage for G's training in the subsequent cycle. After training, $R^*(MR)$ is referred to as `alignMR`, as it evolves from the original MR towards enhanced alignment with pCT. This aligned MR can be further utilized for more precise evaluations, as discussed in Sec.II.F..

Training of G involved an L1 loss calculation between $R^*(MR)$ and CT for each sampled slice, with a batch size of 64 and a learning rate of $2e-4$. The optimization of R incorporated two loss components. The first, denoted as L_{reg} , was the L1 loss calculated between the warped sCT and the pCT, expressed as $L_{reg} = \sum_i \sum_j L1(sCT_i(p_j + \delta p_j), pCT_i(p_j))$. The second component involved regularization over the determinant of the Jacobian matrix for DVF on a per-voxel basis, aiming to maintain values close to 1 to minimize distortion. R was trained with a batch size of 64 and a learning rate of $1e-4$, randomly sampling 64 voxels within the region of interest (RoI) for each case. All training and evaluation were executed on 2 NVIDIA RTX 4090 GPUs.

This alternating optimization strategy was instrumental in ensuring that G accurately captured the anatomical details of the MRs, while R effectively aligned these details with the corresponding CTs. Through iterative refinement of both networks, our framework achieved synergistic enhancements in both the anatomical accuracy of the synthetic CT images and their alignment with planning CTs.

II.D. Dataset

This study employed a dataset comprising images from patients with head-and-neck tumors, treated at PSI between 2017 and 2022. We collected paired MR-CT scans from 60 patients, dividing them into training, validation, and testing sets with respective counts of 40, 8, and 12. Each participant underwent at least one MRI and one CT scan during the pre-treatment planning phase. A significant challenge encountered was the notable anatomical differences between MR and CT scans, largely due to disparate scanning equipment and variations in patient neck positioning during the two scanning sessions. For CT imaging, we used a Siemens Sensation Open CT scanner at a tube voltage of 120kV, achieving image resolutions of $1 \times 1 \times 2$ mm. MR scans were obtained using a 1.5T Siemens Aera MR scanner, with a voxel size of $1 \times 1 \times 1$ mm. Primarily, the T1 vibe Dixon tra sequence was employed for network training purposes. The study was carried out in strict adherence to ethical standards for human data research. Informed consent was obtained from all patients to use their anonymized data in scientific research. Anonymization was meticulously carried out before the analysis phase to ensure patient confidentiality and adherence to ethical standards.

II.E. Preprocessing

Both MR and CT images underwent preprocessing to ensure consistency and optimal quality for training and evaluation. Initially, we applied the Otsu method⁷¹, using SimpleITK¹, to extract Regions of Interest (RoI) masks from each imaging modality. The final valid RoI region for analysis was determined by the intersection of these masks. In the final RoI, voxels outside this region were assigned a value of -1024 HU for CT and 0 for MR to maintain uniformity. MR images were normalized between 0 and 1, with extremities set at the 99.5 and 0.5 percentiles, while CT images were normalized within the Hounsfield unit range of $[-1024, 3072]$.

Subsequent steps involved aligning the MR images to their corresponding CT scans using mutual information-based registration methods in SimpleITK¹, resulting in two sets of images, `rigidMR` and `deformMR`, categorized by applying rigid or deformable registration. These images were resampled to match the CT resolution. For training our 2D generation network, slices were randomly sampled from these preprocessed images along the Z-axis. The training data were augmented per slice as in⁷², involving random rotations within a range of $[-30, 30]$ degrees, resizing factors between 0.7 and 1.3, and random flipping. During testing, MR slices were slices along the Z-axis without augmentation, and the output slices were stacked to reconstruct the synthetic CTs.

II.F. Image-level Evaluation

To ensure a thorough evaluation of the accuracy of our sCT images, we employed a diverse range of evaluation metrics, spanning two key aspects: intensity value mapping accuracy and anatomic conformity. For value mapping accuracy, we utilized Mean Absolute Error (MAE), Peak Signal-to-Noise Ratio (PSNR), and Structural Similarity Index (SSIM). MAE and PSNR calculations were confined to the RoI, while SSIM was calculated over the minimum-circumscribed cuboid of the RoI. To gauge anatomical conformity, we employed Dice Coefficients (Dice) for different regions (e.g. bone: $HU > 250$) and Mutual Information (MI) between pairs of images. Specifically, MI served a dual role: it was used to evaluate the spatial invariance of the generation network by comparing MR and sCT images and to evaluate the efficacy of alignment by comparing different MR registration states `rigidMR/deformMR/alignMR` with the pCT. We plotted example MRs,

¹<https://simpleitk.org/>

pCTs, sCTs, and corresponding error maps to highlight the differences between different methods and evaluation MRs scenarios. In addition, 2D histograms between CT and different MRs were visualized to highlight spatial alignments.

For comparative analysis, we contrasted our proposed alternating methods, rigid→align and deform→align, against conventional sequential approaches using rigidMR (rigid-only) or deformMR (deform-only). These conventional methods involve training G with pre-processed registration between MR and pCT, while the new approaches signify an advance by incorporating the alignment process into the generation training. For evaluation, as the fidelity of pCT and MR was not assured, we employed both deformMR and alignMR as references with respect to the sCT. In particular, alignMR for the test set was generated by hold-out training on a reversed train/val/test split.

II.G. Dosimetric-level Evaluation

The ultimate aim of our work is to synthesize high-quality sCT for adaptive proton therapy. Therefore, dosimetric evaluations were performed on 12 cases with full information on the testing set. To assess the effectiveness of the image synthesis framework, we optimized the plan using the pCT and subsequently recalculated the doses for the sCTs of all scenarios using the Juliana software⁷³. This comparison entailed measuring the Mean Dose Error (MDE) at various dose thresholds (10%, 50%, 90% of the maximum prescribed dose) between the doses optimized for pCT (pDose) and its recalculation for sCTs (sDoses). Additionally, we evaluated the gamma pass rate of pDose and sDoses using three distinct parameter sets (1mm/1%, 2mm/2%, 3mm/3%). To facilitate a more intuitive comparison between pDose and sDoses, we plotted Dose-Volume Histograms (DVHs) of PTVs and OARs and extracted their representative dosimetric indices. Furthermore, our analysis also extends to present the differences in dose indices for both planning target volumes (PTVs) and organs at risk (OARs).

III. Results

The proposed method exhibited good efficiency, with the training completed in only 1.5 hours, thanks to refined code optimization and the adoption of half-precision computation. The inference time for each test case was fast, taking only about 5 seconds per volume. The results presented

in this section include the mean values and standard deviations across the 12 testing cases to provide a comprehensive overview.

III.A. Evaluation for sCT Generation

Table 1: Quantitative comparisons between the proposed methods and conventional ones. The best results are in **bold** and the second best with underlines. Arrows indicate the preference order of a measure. \uparrow / \downarrow denotes higher / lower is better.

Test	Train	MAE (HU) \downarrow	PSNR (dB) \uparrow	SSIM (%) \uparrow	Dice (%) \uparrow	MI (%) \uparrow
deformMR	rigid-only	157.75 \pm 19.01	22.00 \pm 0.87	69.02 \pm 4.00	51.87 \pm 6.69	67.65 \pm 3.83
	deform-only	124.95 \pm 30.74	23.78 \pm 1.53	73.81 \pm 4.44	67.78 \pm 12.60	72.26 \pm 4.69
	rigid \rightarrow align	136.49 \pm 28.16	22.87 \pm 1.27	73.16 \pm 4.40	59.83 \pm 9.78	71.90 \pm 4.56
	deform \rightarrow align	115.65 \pm 33.87	24.31 \pm 1.77	76.42 \pm 4.86	68.14 \pm 12.66	74.55 \pm 5.01
alignMR	rigid-only	164.02 \pm 14.93	21.71 \pm 0.70	68.28 \pm 3.77	50.39 \pm 4.48	66.87 \pm 3.88
	deform-only	111.36 \pm 8.86	<u>24.59\pm0.67</u>	74.60 \pm 2.95	<u>74.34\pm4.29</u>	71.87 \pm 4.74
	rigid \rightarrow align	<u>109.52\pm9.66</u>	24.51 \pm 0.68	<u>76.62\pm2.95</u>	68.37 \pm 3.44	<u>72.09\pm4.68</u>
	deform \rightarrow align	80.98\pm7.55	27.13\pm0.85	81.14\pm2.70	79.48\pm3.70	74.74\pm5.10

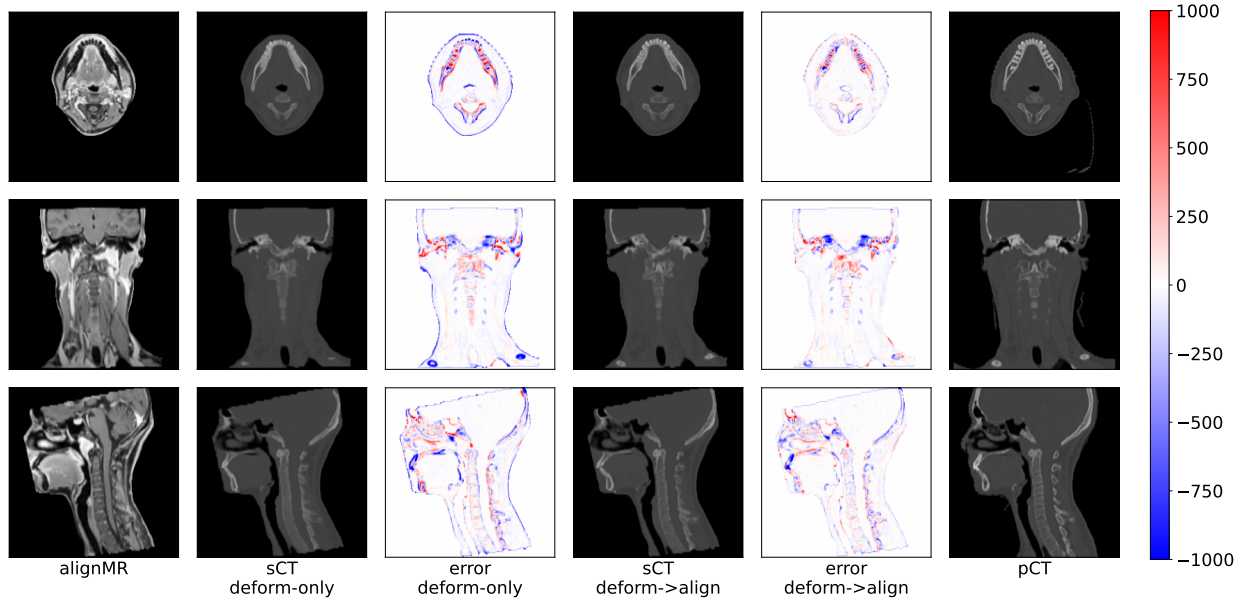


Figure 2: Visual comparisons of sCTs and error maps from deform-only and deform \rightarrow align evaluated on alignMR. The error map was computed as sCT - pCT.

To assess the image generation performance, as a baseline reference, the conventional deform-only method, when evaluated on deformMR, resulted in an MAE of 124.95 ± 30.74 HU and a Dice score of $67.78 \pm 12.60\%$ in the bone region across 12 test cases. Our proposed deform \rightarrow align method, evaluated on the same deformMR, demonstrated an improved MAE of

115.65 ± 33.87 HU and a marginally higher Dice score of $68.14 \pm 12.66\%$. Notably, the performance difference was more pronounced when tested on alignMR, which is considered as better aligned MR images to pCT. Here, the MAE for deform→align significantly reduced to 80.98 ± 7.55 HU, with the Dice score increasing to $79.48 \pm 3.70\%$. A similar pattern was observed in the comparison of rigid-only with rigid→align, as detailed in Table.1. In Fig.2, we visually compared sCTs generated by different methods with respect to alignMR, along with their corresponding error maps. More comprehensive results of MAE and Dice in different regions (air: $HU < -200$, tissue: $-200 \leq HU \leq 250$, bone: $HU > 250$) are presented in Tables 3&4 of the Appendices. Additional visual results are available in Figures 1&2 of the Supplementary Materials.

III.B. Alignment Evaluation

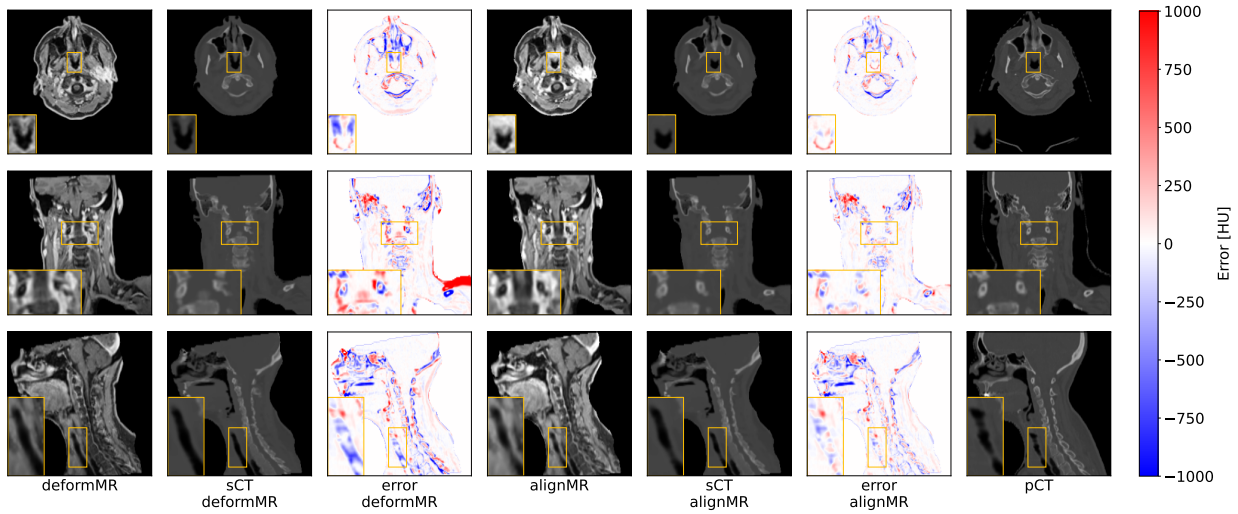


Figure 3: Visual results of sCTs and error maps from deform→align on different MRs.

The mutual information (MI) metrics further demonstrated the improvement of the paired images. The MI between input MR and pCT was $63.12 \pm 3.75\%$ for rigidMR, $67.76 \pm 4.46\%$ for deformMR, and significantly higher of $69.82 \pm 4.49\%$ for alignMR. This increasing trend in MI scores emphasizes the superior alignment achieved through our comprehensive registration approach. The refined alignment in alignMR led to fewer misalignments in the sCTs, allowing for a more precise comparison in terms of MAE and Dice scores as reported above. Fig.3 displays sCTs generated by the deform→align method across various MR alignment states. Notably, rigid→align demonstrated comparable performance to deform-only when evaluated on alignMR, indicating

that a single training session on both generation and registration can match the performance of the conventional sequential deformable registration followed by generation training. Figure 4 presents joint histograms of MR-to-CT values, where alignMR exhibits a narrower distribution in the high CT value region compared to both rigidMR and deformMR.

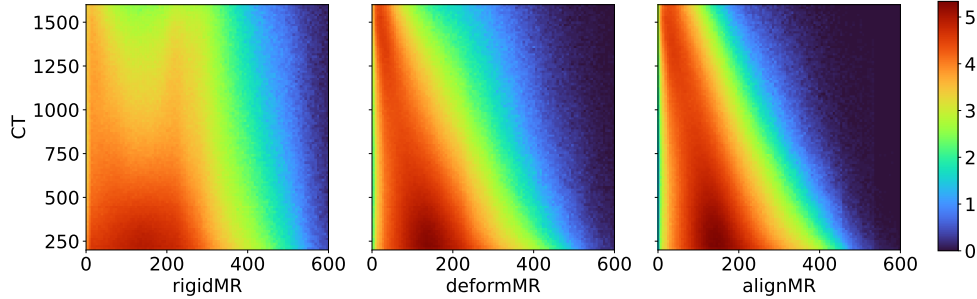


Figure 4: Corresponding MR-to-CT log-scale joint histogram over bone regions. A narrower distribution corresponds to a higher MI value.

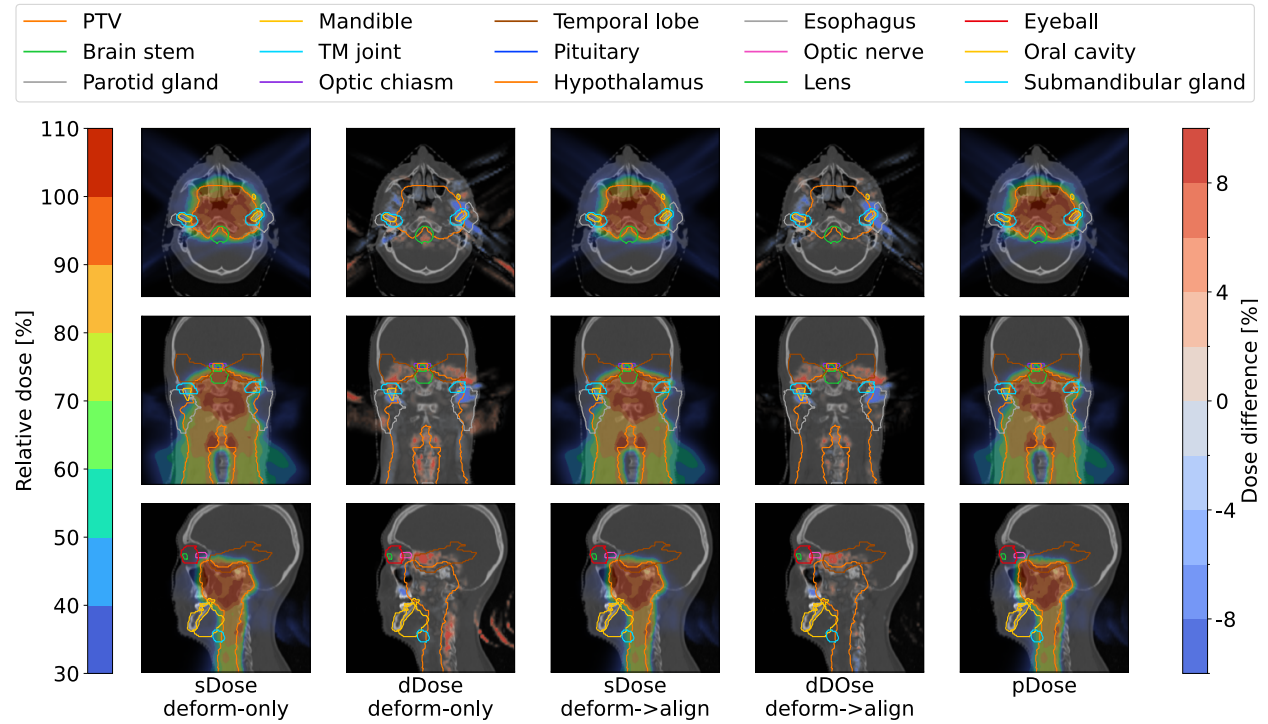
III.C. Dosimetric-level Evaluation

Table 2: Gamma pass rate (%) of sDoses from different methods over different thresholds.

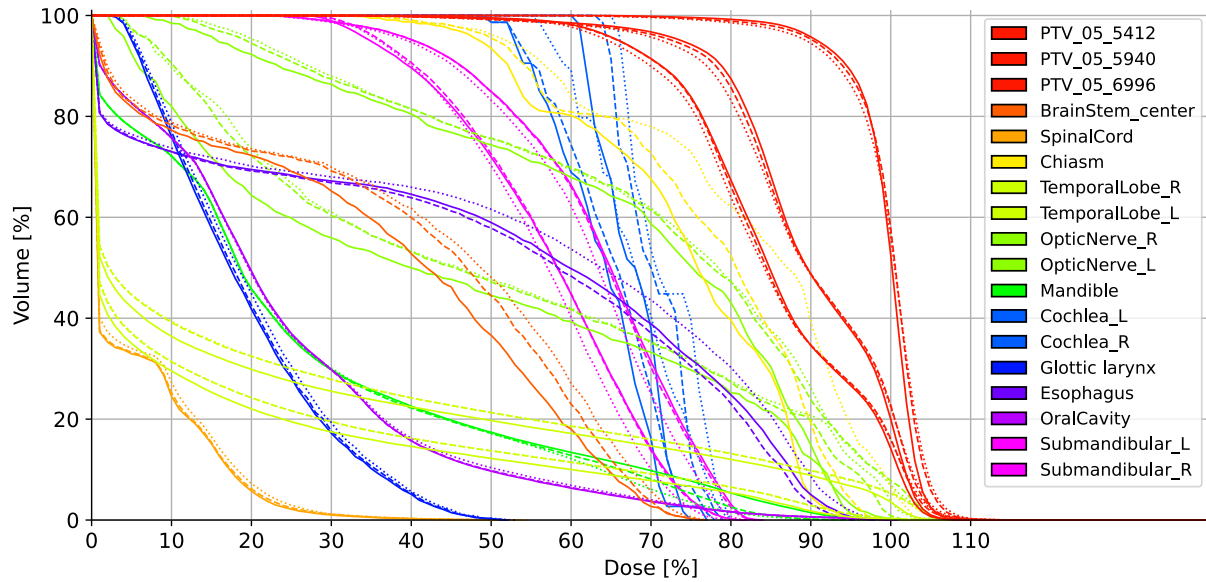
Testing	Training	1mm/1%	2mm/2%	3mm/3%
deformMR	rigid-only	91.13 \pm 5.71	95.55 \pm 3.34	97.50 \pm 2.09
	deform-only	92.73 \pm 5.10	96.58 \pm 2.84	98.17 \pm 1.69
	rigid \rightarrow align	93.40 \pm 5.09	96.62 \pm 3.19	97.99 \pm 2.27
	deform \rightarrow align	93.83 \pm 4.94	96.93 \pm 3.08	98.21 \pm 2.24
alignMR	rigid-only	91.01 \pm 5.45	95.60 \pm 3.16	97.59 \pm 1.93
	deform-only	93.01 \pm 4.66	96.99 \pm 2.41	98.50 \pm 1.32
	rigid \rightarrow align	95.04 \pm 3.79	97.79 \pm 1.90	98.86 \pm 1.05
	deform \rightarrow align	95.85\pm3.31	98.24\pm1.63	99.11\pm0.94

Mean voxel-wise differences of the dose distribution on the body region calculated on the sCT generated by deform \rightarrow align were less than 0.01% of the prescribed dose when evaluated on alignMR. As a comparison, conventional deform-only achieved a dose error rate of around 0.14% on both deformMR and alignMR. More detailed results on dose error rates are shown in Table. 5. With respect to the Gamma pass rate, the proposed method achieved 99.11 \pm 0.94 given the threshold 3mm/3%. Gamma pass rates for different, more strict tolerances are also shown in Table. 2. Visual comparisons of one example case on sDoses and dDoses (sDose - pDose) are shown in Fig.5.a, between deform-only and deform \rightarrow align, with associated DVHs shown in Fig.5.b. Furthermore, the differences of various dosimetric indexes for the PTV and OARs

between sDose and pDose are plotted in Fig.6, where the four method scenarios were compared laterally. Visualization of more cases can be found in Fig 3&4 in the Supporting Materials.



a. Comparison of dose distribution. dDose was calculated as sDose - pDose.



b. Comparison of DVHs. DVHs of pDoses were shown in solid lines, DVHs of deform-only in dotted (...) lines while deform->align was labeled with dashdot lines (- - -)

Figure 5: Comparison of dose distribution and DVHs between conventional method deform-only and the proposed deform->align.

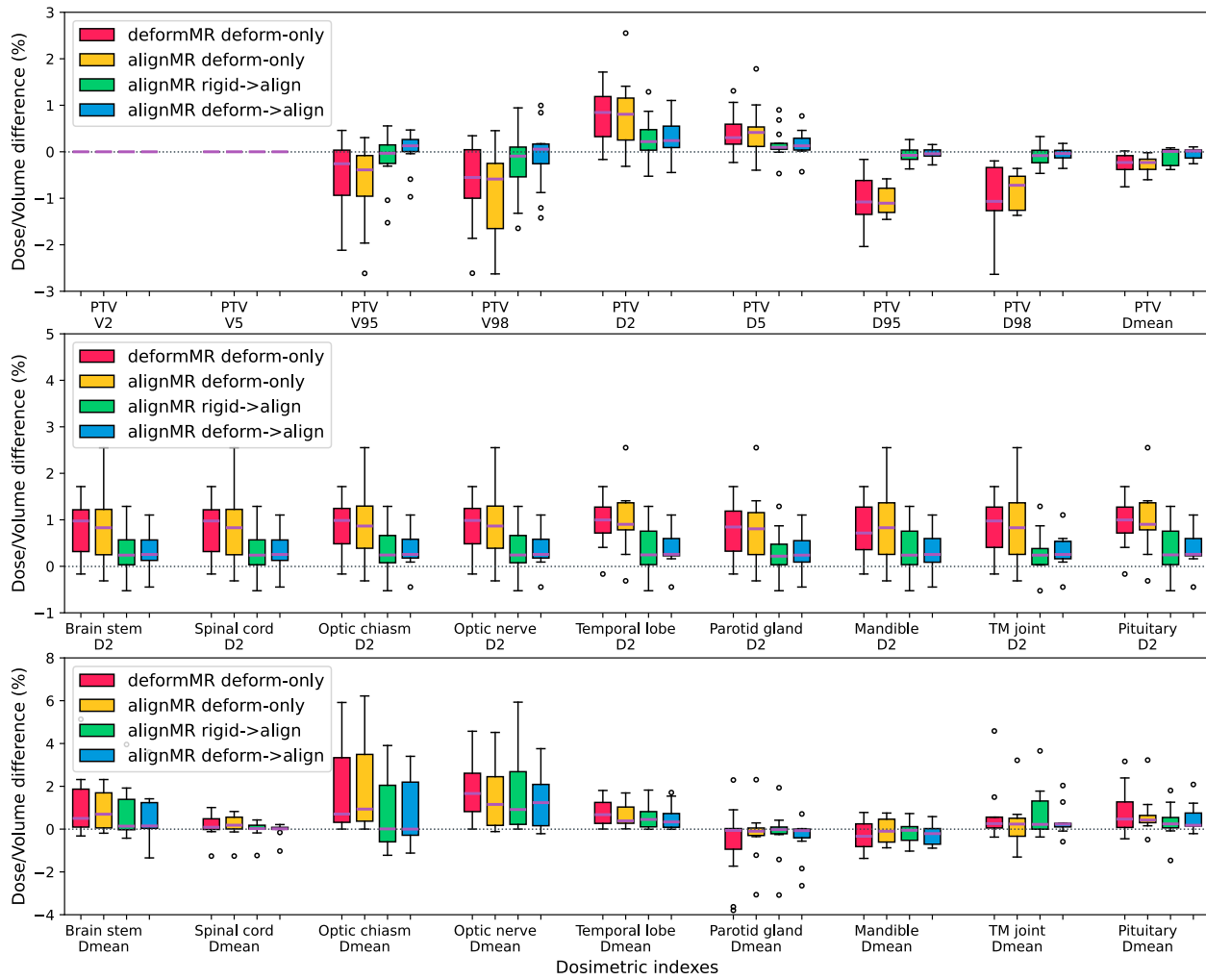


Figure 6: Distributions of dosimetric index differences, compared across different settings. (Boxplot derived from the evaluations of all 12 testing patient cases).

IV. Discussion

Our study evaluates the feasibility and advantages of an alternated image generation and registration framework for synthesizing CTs from MRI in the head-and-neck region for proton therapy. We addressed the complex inter-dependency between MR-based CT synthesis and MR-CT deformable registration. This approach is crucial for expanding MR-based CT synthesis regions where anatomy can deform considerably between the two imaging modalities. By solving the misalignment issue during generation training and evaluation, our method is particularly suited for challenging areas like the head-and-neck.

Registering MR and CT images poses considerable challenges, especially in deformation-prone areas like the head-and-neck region. These challenges are accentuated by inherent discrepancies in coordinates, resolution, and scanning position between MR and CT modalities. Furthermore, differences in texture and contrast between these scans add extra complexity. These factors not only complicate the multi-modality deformable registration process but also determine the training of generation networks. Techniques such as CycleGAN, useful for unpaired data, have performance limitations compared to Pix2Pix at a certain alignment level^{24,58,59}. Similarly, Pix2Pix, preferred for its fidelity in matched pairs, still struggles with pixel-to-pixel misalignments of the two images, leading to overly smooth inferred sCT or spatial biases when trained with isotropic or directional misalignments, respectively. Addressing these issues is essential, as accurate registration plays a pivotal role in the practical evaluation of generation networks, ensuring that the quality of sCT images is not compromised by alignment errors. Although some works using the paired images from the integrated MR-Linac system can inherently benefit from the more aligned dataset thanks to the dedicated fixation device between MR and CT imaging⁵¹, this newly proposed framework would contribute greatly for those centers that have only out-room MR system.

Our methodology introduces a novel integrated approach, combining generation and registration networks into a cohesive framework. This unified translation-registration model improves the alignment between MR and CT images, thereby enhancing the anatomical accuracy of sCT generation. By alternatively optimizing G and R, our method addresses the challenges of conventional techniques that treat image generation and registration as separate sequential entities. This approach ensures that the generation network focuses more effectively on the nuances of intensity mapping, while the registration network aligns the images with high precision. This leads

to the generated sCT images being more accurate in terms of electron density representation and superior anatomical conformity, both essential for precise radiotherapy planning.

Moreover, we strategically decided to align MR images with pCT images instead of the reverse. This choice was crucial for preserving the integrity and consistency of the training process. At early stages of training, sCT images have inferior quality and are often blurred; therefore, aligning them to fine-detailed MR images is safer than the opposite direction. The reversed choice, as employed in the study cited by⁵³, presents a risk: fine details in pCT, such as streaks and spots, might be lost when registered to the smoother sCT, and this transformation is irreversible. When tested on our alignMR, the reverse process of `deform⇒align` yielded worse MAE at 105.15 ± 6.97 HU, PSNR at 25.36 ± 0.57 dB, SSIM at $93.95 \pm 0.84\%$, bone Dice at $76.51 \pm 3.21\%$, thereby significantly underperforming compared to the results reported in the last row of Table 1.

Our registration network adopts an INR approach⁶⁹ for **fitting** DVFs, a significant departure from all classic DL methods that typically rely on 2D registration networks⁷⁴ or 3D low-resolution networks for **predicting** DVFs from paired inputs⁴¹. By employing a shared network with unique latent vectors for each case, our method efficiently captures the required deformations while minimizing demands on memory and storage. With its compact 4MB network size, this approach offers a scalable and practical solution in medical imaging. Direct fitting of DVF volumes, though appearing to be feasible, tends to lack efficiency due to slow convergence and high demands on memory (100MB+). This efficiency from our choice is particularly advantageous in handling large medical image datasets, ensuring that our method is not only effective in capturing essential deformation information but also practical for real-world clinical applications.

Evaluating the quality of sCT images using non-aligned MR-CT pairs adds complexity to the analysis. The proposed approach can conflate errors from the value mapping process with those arising from alignment inaccuracies. By integrating registration with generation, our method minimizes such conflated errors, focusing more accurately on the quality of value mapping. However, potential convergence issues remain a concern, where the generation network might learn incorrect mappings along with spatial shifts, and the registration network could inadvertently correct these shifts, leading to low training errors but inaccurate predictions. Additionally, the use of MI as a primary metric for alignment evaluation has its limitations, as it does not fully capture the nuances of anatomical alignment, nor does it provide an explicit upper bound for registration

quality. Furthermore, it remains challenging to ascertain the exact degree to which our alignMR could be considered an “ideal” aligned MR, leaving room for further future exploration in this aspect of this method.

MR-based dose planning presents unique challenges due to the discrepancies in the Field of View (FOV) between MR and CT scans. Typically, out-room MR imaging focuses on a narrower FOV, primarily covering the Gross Tumor Volume (GTV) and its surroundings, whereas CT scans cover the full area, including the complete lymph nodes in the neck region. This difference poses challenges in ensuring comprehensive coverage in MR-based synthetic CT generation, which is critical for bridging the gap between experimental settings and practical clinical applications⁴⁹. In the dosimetric evaluation of this work, we chose to pad sCT to the full CT lending values from pCT, which may influence the performance measurements. Regarding the dose planning approach, we opted to optimize on pCT and recalculate on sCTs. Although the alternative approach of optimizing on sCT and recalculating on pCTs closely mirrors real-case scenarios where only MR is available, our choice aligns enough with our objective of effectively evaluating our synthesis framework, providing comparable data from both pCT and sCT for a more accurate assessment.

Finally, the definition of masks used in evaluation metrics like Mean Absolute Error (MAE) significantly influences the outcomes of our comparisons. Variations in mask definitions across different studies, such as using a strict body mask or an expanded mask to include more tissue types, make direct comparisons of MAE values challenging. This variability highlights the need for standardized evaluation protocols in medical imaging research. Such standardization would ensure fair and accurate comparisons between methodologies, particularly on public datasets with pre-defined metrics. Addressing these discrepancies is vital for advancing the field and enhancing research findings’ reliability and clinical relevance. In this regard, SynthRAD⁷⁵ has made a significant step forward.

V. Conclusion

In this study, we developed an approach that substantially improves the anatomical accuracy of synthetic CT (sCT) images for MR-based radiotherapy planning. By integrating image generation with the deformable registration processes, the novel framework effectively addresses the inherent

challenges in MR-CT registration and sCT evaluation. The methodological synergy of generation and registration networks, coupled with a strategic approach to proton dose planning, contributes to enhancing treatment planning accuracy. This study represents a meaningful step forward in the application of MR-based proton treatment planning and daily adaptive replanning, offering potential improvements in reducing the imaging-related dose and patient outcomes in the field of radiotherapy.

Acknowledgments

This project is supported by the interdisciplinary doctoral grant (iDoc 2021-360) from the Personalized Health and Related Technologies (PHRT) of the ETH domain, Switzerland. The automatic planning system used in this work was developed as part of the EU-H2020 project ‘INSPIRE’ (InfraStructure in Proton International REsearch; grant ID: 730983)

Appendix

More Quantitative Analysis

Table 3: MAE values (HU) from different methods over different regions.

Testing	Training	MAE_body	MAE_air	MAE_tissue	MAE_bone
deformMR	rigid-only	157.16±19.01	387.20±48.59	86.40±9.36	565.60±62.59
	deform-only	124.85±30.74	329.58±74.43	71.69±17.24	412.87±93.90
	rigid→align	136.49±28.16	367.36±103.38	71.98±15.04	492.67±71.71
	deform→align	115.65±33.87	335.77±96.60	61.79±19.14	401.12±95.03
alignMR	rigid-only	164.02±14.93	402.96±37.35	91.03±6.02	583.58±54.92
	deform-only	111.36±8.86	306.05±40.63	64.38±3.77	<u>365.25±31.67</u>
	rigid→align	<u>109.52±9.66</u>	<u>288.54±47.73</u>	<u>54.40±4.24</u>	427.30±34.29
	deform→align	80.98±7.55	251.89±39.61	41.63±2.89	290.21±24.53

Table 4: Dices scores (%) from different methods over different regions.

Testing	Training	Dice_mean	Dice_air	Dice_tissue	Dice_bone
deformMR	rigid-only	65.02±3.40	52.08±3.92	91.11±1.21	51.87±7.62
	deform-only	73.66±6.49	59.90±6.10	93.29±1.99	67.78±12.60
	rigid→align	71.21±7.08	60.83±10.26	92.97±1.90	59.83±9.78
	deform→align	75.77±7.85	65.07±9.35	94.08±2.18	68.14±12.66
alignMR	rigid-only	63.17±2.28	48.51±3.88	90.62±0.80	50.39±4.48
	deform-only	76.06±2.35	59.75±4.48	94.09±0.60	<u>74.34±4.29</u>
	rigid→align	<u>78.19±2.08</u>	<u>71.59±4.39</u>	<u>94.63±0.54</u>	68.37±3.44
	deform→align	83.85±2.05	75.93±3.66	96.14±0.56	79.48±3.70

Table 5: Mean Dose Error (%) from different methods by different thresholds.

Testing	Training	Dose _{body}	Dose>10%	Dose>50%	Dose>90%
deformMR	rigid-only	0.18±0.19	0.23±0.25	0.09±0.67	-0.15±0.62
	deform-only	0.14±0.12	0.15±0.19	0.12±0.46	0.04±0.36
	rigid→align	0.02±0.12	-0.03±0.28	-0.11±0.53	-0.12±0.44
	deform→align	0.03±0.09	-0.02±0.25	-0.07±0.46	-0.06±0.39
alignMR	rigid-only	0.18±0.17	0.24±0.24	0.10±0.63	-0.18±0.60
	deform-only	0.14±0.12	0.20±0.17	0.18±0.39	0.04±0.39
	rigid→align	0.00±0.09	-0.01±0.14	-0.05±0.36	-0.07±0.35
	deform→align	0.00±0.06	-0.01±0.12	-0.02±0.24	-0.00±0.23

References

- ¹ H. Paganetti et al., Roadmap: proton therapy physics and biology, *Phys. Med. Biol.* **66**, 05RM01 (2021).
- ² R. Kashani and J. R. Olsen, Magnetic resonance imaging for target delineation and daily treatment modification, in *Seminars in radiation oncology*, volume 28, pages 178–184, Elsevier, 2018.
- ³ F. Albertini, M. Matter, L. Nenoff, Y. Zhang, and A. Lomax, Online daily adaptive proton therapy, *The British journal of radiology* **93**, 20190594 (2020).
- ⁴ A. Hoffmann et al., MR-guided proton therapy: a review and a preview, *Radiation Oncology* **15**, 1–13 (2020).
- ⁵ R. Liu et al., Synthetic dual-energy CT for MRI-only based proton therapy treatment planning using label-GAN, *Phys. Med. Biol.* **66**, 065014 (2021).
- ⁶ X. Han, MR-based synthetic CT generation using a deep convolutional neural network method, *Med. Phys.* **44**, 1408–1419 (2017).
- ⁷ A. Thummerer et al., Comparison of the suitability of CBCT-and MR-based synthetic CTs for daily adaptive proton therapy in head and neck patients, *Phys. Med. Biol.* **65**, 235036 (2020).
- ⁸ B. Rigaud et al., Evaluation of deformable image registration methods for dose monitoring in head and neck radiotherapy, *BioMed research international* **2015** (2015).

- ⁹ H. Arabi, J. A. Dowling, N. Burgos, X. Han, P. B. Greer, N. Koutsouvelis, and H. Zaidi, Comparative study of algorithms for synthetic CT generation from MRI: consequences for MRI-guided radiation planning in the pelvic region, *Med. Phys.* **45**, 5218–5233 (2018).
 - ¹⁰ S. Chen, A. Qin, D. Zhou, and D. Yan, U-net-generated synthetic CT images for magnetic resonance imaging-only prostate intensity-modulated radiation therapy treatment planning, *Med. Phys.* **45**, 5659–5665 (2018).
 - ¹¹ A. Bahrami, A. Karimian, E. Fatemizadeh, H. Arabi, and H. Zaidi, A new deep convolutional neural network design with efficient learning capability: Application to CT image synthesis from MRI, *Med. Phys.* **47**, 5158–5171 (2020).
 - ¹² M. Maspero, M. H. Savenije, A. M. Dinkla, P. R. Seevinck, M. P. Intven, I. M. Jurgenliemk-Schulz, L. G. Kerkmeijer, and C. A. van den Berg, Dose evaluation of fast synthetic-CT generation using a generative adversarial network for general pelvis MR-only radiotherapy, *Phys. Med. Biol.* **63**, 185001 (2018).
 - ¹³ H. Emami, M. Dong, S. P. Nejad-Davarani, and C. K. Glide-Hurst, Generating synthetic CTs from magnetic resonance images using generative adversarial networks, *Med. Phys.* **45**, 3627–3636 (2018).
 - ¹⁴ M. Qi et al., Multi-sequence MR image-based synthetic CT generation using a generative adversarial network for head and neck MRI-only radiotherapy, *Med. Phys.* **47**, 1880–1894 (2020).
 - ¹⁵ X. Tie, S.-K. Lam, Y. Zhang, K.-H. Lee, K.-H. Au, and J. Cai, Pseudo-CT generation from multi-parametric MRI using a novel multi-channel multi-path conditional generative adversarial network for nasopharyngeal carcinoma patients, *Med. Phys.* **47**, 1750–1762 (2020).
 - ¹⁶ J. E. Scholey, A. Rajagopal, E. G. Vasquez, A. Sudhyadhom, and P. E. Z. Larson, Generation of synthetic megavoltage CT for MRI-only radiotherapy treatment planning using a 3D deep convolutional neural network, *Med. Phys.* **49**, 6622–6634 (2022).
 - ¹⁷ H. A. Massa, J. M. Johnson, and A. B. McMillan, Comparison of deep learning synthesis of synthetic CTs using clinical MRI inputs, *Phys. Med. Biol.* **65**, 23NT03 (2020).
-

-
- ¹⁸ A. B. Olin et al., Feasibility of multiparametric positron emission tomography/magnetic resonance imaging as a one-stop shop for radiation therapy planning for patients with head and neck cancer, *International Journal of Radiation Oncology Biology Physics* **108**, 1329–1338 (2020).
- ¹⁹ S. Kaushik et al., Region of interest focused mri to synthetic ct translation using regression and classification multi-task network, *arXiv preprint arXiv:2203.16288* (2022).
- ²⁰ J. J. Wyatt et al., Comprehensive dose evaluation of a Deep Learning based synthetic Computed Tomography algorithm for pelvic Magnetic Resonance-only radiotherapy, *Radiotherapy and Oncology* **184**, 109692 (2023).
- ²¹ D. Cusumano et al., A deep learning approach to generate synthetic CT in low field MR-guided adaptive radiotherapy for abdominal and pelvic cases, *Radiotherapy and Oncology* **153**, 205–212 (2020).
- ²² A. M. Dinkla, M. C. Florkow, M. Maspero, M. H. Savenije, F. Zijlstra, P. A. Doornaert, M. van Stralen, M. E. Philippens, C. A. van den Berg, and P. R. Seevinck, Dosimetric evaluation of synthetic CT for head and neck radiotherapy generated by a patch-based three-dimensional convolutional neural network, *Med. Phys.* **46**, 4095–4104 (2019).
- ²³ J. Fu, Y. Yang, K. Singhrao, D. Ruan, F.-I. Chu, D. A. Low, and J. H. Lewis, Deep learning approaches using 2D and 3D convolutional neural networks for generating male pelvic synthetic computed tomography from magnetic resonance imaging, *Med. Phys.* **46**, 3788–3798 (2019).
- ²⁴ P. Klages, I. Benslimane, S. Riyahi, J. Jiang, M. Hunt, J. O. Deasy, H. Veeraraghavan, and N. Tyagi, Patch-based generative adversarial neural network models for head and neck MR-only planning, *Med. Phys.* **47**, 626–642 (2020).
- ²⁵ A. M. Dinkla, M. C. Florkow, M. Maspero, M. H. Savenije, F. Zijlstra, P. A. Doornaert, M. van Stralen, M. E. Philippens, C. A. van den Berg, and P. R. Seevinck, Dosimetric evaluation of synthetic CT for head and neck radiotherapy generated by a patch-based three-dimensional convolutional neural network, *Med. Phys.* **46**, 4095–4104 (2019).
- ²⁶ M. Maspero, L. G. Bentvelzen, M. H. Savenije, F. Guerreiro, E. Seravalli, G. O. Janssens, C. A. van den Berg, and M. E. Philippens, Deep learning-based synthetic CT generation for
-

- paediatric brain MR-only photon and proton radiotherapy, *Radiotherapy and Oncology* **153**, 197–204 (2020).
- ²⁷ M. F. Spadea, G. Pileggi, P. Zaffino, P. Salome, C. Catana, D. Izquierdo-Garcia, F. Amato, and J. Seco, Deep convolution neural network (DCNN) multiplane approach to synthetic CT generation from MR images—application in brain proton therapy, *International Journal of Radiation Oncology* Biology* Physics* **105**, 495–503 (2019).
- ²⁸ S. Olberg et al., Synthetic CT reconstruction using a deep spatial pyramid convolutional framework for MR-only breast radiotherapy, *Med. Phys.* **46**, 4135–4147 (2019).
- ²⁹ Y. Liu et al., MRI-based treatment planning for proton radiotherapy: dosimetric validation of a deep learning-based liver synthetic CT generation method, *Phys. Med. Biol.* **64**, 145015 (2019).
- ³⁰ A. M. Dinkla, J. M. Wolterink, M. Maspero, M. H. Savenije, J. J. Verhoeff, E. Seravalli, I. Išgum, P. R. Seevinck, and C. A. van den Berg, MR-only brain radiation therapy: dosimetric evaluation of synthetic CTs generated by a dilated convolutional neural network, *International Journal of Radiation Oncology* Biology* Physics* **102**, 801–812 (2018).
- ³¹ L. Xiang, Q. Wang, D. Nie, L. Zhang, X. Jin, Y. Qiao, and D. Shen, Deep embedding convolutional neural network for synthesizing CT image from T1-Weighted MR image, *Medical image analysis* **47**, 31–44 (2018).
- ³² B. Zhao, T. Cheng, X. Zhang, J. Wang, H. Zhu, R. Zhao, D. Li, Z. Zhang, and G. Yu, CT synthesis from MR in the pelvic area using Residual Transformer Conditional GAN, *Computerized Medical Imaging and Graphics* **103**, 102150 (2023).
- ³³ R. Touati, W. T. Le, and S. Kadoury, A feature invariant generative adversarial network for head and neck MRI/CT image synthesis, *Phys. Med. Biol.* **66**, 095001 (2021).
- ³⁴ H. Sun, Q. Xi, R. Fan, J. Sun, K. Xie, X. Ni, and J. Yang, Synthesis of pseudo-CT images from pelvic MRI images based on an MD-CycleGAN model for radiotherapy, *Phys. Med. Biol.* **67**, 035006 (2022).
- ³⁵ L. Fetty, T. Löfstedt, G. Heilemann, H. Furtado, N. Nesvacil, T. Nyholm, D. Georg, and P. Kuess, Investigating conditional GAN performance with different generator architectures,
-

- an ensemble model, and different MR scanners for MR-sCT conversion, *Phys. Med. Biol.* **65**, 105004 (2020).
- ³⁶ A. Largent et al., Comparison of deep learning-based and patch-based methods for pseudo-CT generation in MRI-based prostate dose planning, *International Journal of Radiation Oncology* Biology* Physics* **105**, 1137–1150 (2019).
- ³⁷ D. Nie, R. Trullo, J. Lian, L. Wang, C. Petitjean, S. Ruan, Q. Wang, and D. Shen, Medical image synthesis with deep convolutional adversarial networks, *IEEE Transactions on Biomedical Engineering* **65**, 2720–2730 (2018).
- ³⁸ S. Kazemifar, S. McGuire, R. Timmerman, Z. Wardak, D. Nguyen, Y. Park, S. Jiang, and A. Owrangi, MRI-only brain radiotherapy: Assessing the dosimetric accuracy of synthetic CT images generated using a deep learning approach, *Radiotherapy and Oncology* **136**, 56–63 (2019).
- ³⁹ X. Liang et al., Bony structure enhanced synthetic CT generation using Dixon sequences for pelvis MR-only radiotherapy, *Med. Phys.* (2023).
- ⁴⁰ E. A. Andres et al., Dosimetry-driven quality measure of brain pseudo computed tomography generated from deep learning for MRI-only radiation therapy treatment planning, *International Journal of Radiation Oncology* Biology* Physics* **108**, 813–823 (2020).
- ⁴¹ S. Reaungamornrat, H. Sari, C. Catana, and A. Kamen, Multimodal image synthesis based on disentanglement representations of anatomical and modality specific features, learned using uncooperative relativistic GAN, *Medical image analysis* **80**, 102514 (2022).
- ⁴² S. Pan et al., 2D medical image synthesis using transformer-based denoising diffusion probabilistic model, *Phys. Med. Biol.* **68**, 105004 (2023).
- ⁴³ L. Liu, A. Johansson, Y. Cao, J. Dow, T. S. Lawrence, and J. M. Balter, Abdominal synthetic CT generation from MR Dixon images using a U-net trained with 'semi-synthetic'CT data, *Phys. Med. Biol.* **65**, 125001 (2020).
- ⁴⁴ M. C. Florkow et al., Deep learning-enabled MRI-only photon and proton therapy treatment planning for paediatric abdominal tumours, *Radiotherapy and Oncology* **153**, 220–227 (2020).
-

- ⁴⁵ C. Wang, J. Uh, T. Patni, T. Merchant, Y. Li, C.-h. Hua, and S. Acharya, Toward MR-only proton therapy planning for pediatric brain tumors: Synthesis of relative proton stopping power images with multiple sequence MRI and development of an online quality assurance tool, *Med. Phys.* **49**, 1559–1570 (2022).
- ⁴⁶ S. Zhao, C. Geng, C. Guo, F. Tian, and X. Tang, SARU: A self-attention ResUNet to generate synthetic CT images for MR-only BNCT treatment planning, *Med. Phys.* **50**, 117–127 (2023).
- ⁴⁷ K. N. B. Boni, J. Klein, L. Vanquin, A. Wagner, T. Lacornerie, D. Pasquier, and N. Reynaert, MR to CT synthesis with multicenter data in the pelvic area using a conditional generative adversarial network, *Phys. Med. Biol.* **65**, 075002 (2020).
- ⁴⁸ D. Bird et al., Multicentre, deep learning, synthetic-CT generation for ano-rectal MR-only radiotherapy treatment planning, *Radiotherapy and Oncology* **156**, 23–28 (2021).
- ⁴⁹ Y. Zhao, H. Wang, C. Yu, L. E. Court, X. Wang, Q. Wang, T. Pan, Y. Ding, J. Phan, and J. Yang, Compensation cycle consistent generative adversarial networks (Comp-GAN) for synthetic CT generation from MR scans with truncated anatomy, *Med. Phys.* (2023).
- ⁵⁰ S. Olberg, J. Chun, B. S. Choi, I. Park, H. Kim, T. Kim, J. S. Kim, O. Green, and J. C. Park, Abdominal synthetic CT reconstruction with intensity projection prior for MRI-only adaptive radiotherapy, *Phys. Med. Biol.* **66**, 204001 (2021).
- ⁵¹ M. G. K. YJMdH, M. Maspero, C. Kontaxis, S. Mandija, J. Vasmel, R. Charaghvandi, M. Philippens, B. van Asselen, and H. van den Bongard, Synthetic CT for single-fraction neoadjuvant partial breast irradiation on an MRI-linac, *Phys Med Biol* **20121**, 66.
- ⁵² H. Hooshangnejad, Q. Chen, X. Feng, R. Zhang, and K. Ding, deepPERFECT: Novel Deep Learning CT Synthesis Method for Expeditious Pancreatic Cancer Radiotherapy, *Cancers* **15**, 3061 (2023).
- ⁵³ L. Zhou, X. Ni, Y. Kong, H. Zeng, M. Xu, J. Zhou, Q. Wang, and C. Liu, Mitigating misalignment in MRI-to-CT synthesis for improved synthetic CT generation: an iterative refinement and knowledge distillation approach, *Phys. Med. Biol.* (2023).
-

-
- ⁵⁴ Y. Lei, J. Harms, T. Wang, Y. Liu, H.-K. Shu, A. B. Jani, W. J. Curran, H. Mao, T. Liu, and X. Yang, MRI-only based synthetic CT generation using dense cycle consistent generative adversarial networks, *Med. Phys.* **46**, 3565–3581 (2019).
- ⁵⁵ J. Wang, B. Yan, X. Wu, X. Jiang, Y. Zuo, and Y. Yang, Development of an unsupervised cycle contrastive unpaired translation network for MRI-to-CT synthesis, *Journal of Applied Clinical Medical Physics* **23**, e13775 (2022).
- ⁵⁶ K. N. Brou Boni, J. Klein, A. Gulyban, N. Reynaert, and D. Pasquier, Improving generalization in MR-to-CT synthesis in radiotherapy by using an augmented cycle generative adversarial network with unpaired data, *Med. Phys.* **48**, 3003–3010 (2021).
- ⁵⁷ H. Yang, J. Sun, A. Carass, C. Zhao, J. Lee, J. L. Prince, and Z. Xu, Unsupervised MR-to-CT synthesis using structure-constrained CycleGAN, *IEEE transactions on medical imaging* **39**, 4249–4261 (2020).
- ⁵⁸ Y. Peng et al., Magnetic resonance-based synthetic computed tomography images generated using generative adversarial networks for nasopharyngeal carcinoma radiotherapy treatment planning, *Radiotherapy and Oncology* **150**, 217–224 (2020).
- ⁵⁹ A. V. Galapon Jr, A. Thummerer, J. A. Langendijk, D. Wagenaar, and S. Both, Feasibility of Monte Carlo dropout-based uncertainty maps to evaluate deep learning-based synthetic CTs for adaptive proton therapy, *Med. Phys.* (2023).
- ⁶⁰ E. M. McKenzie, A. Santhanam, D. Ruan, D. O'Connor, M. Cao, and K. Sheng, Multi-modality image registration in the head-and-neck using a deep learning-derived synthetic CT as a bridge, *Med. Phys.* **47**, 1094–1104 (2020).
- ⁶¹ R. Han et al., Joint synthesis and registration network for deformable MR-CBCT image registration for neurosurgical guidance, *Phys. Med. Biol.* **67**, 125008 (2022).
- ⁶² V. Sitzmann, J. Martel, A. Bergman, D. Lindell, and G. Wetzstein, Implicit neural representations with periodic activation functions, *Advances in neural information processing systems* **33**, 7462–7473 (2020).
- ⁶³ J. M. Wolterink, J. C. Zwienenberg, and C. Brune, Implicit neural representations for deformable image registration, in *International Conference on Medical Imaging with Deep Learning*, pages 1349–1359, PMLR, 2022.
-

- ⁶⁴ F. Isensee et al., nnu-net: Self-adapting framework for u-net-based medical image segmentation, arXiv preprint arXiv:1809.10486 (2018).
- ⁶⁵ X. Cao, J. Yang, L. Wang, Z. Xue, Q. Wang, and D. Shen, Deep learning based inter-modality image registration supervised by intra-modality similarity, in *Machine Learning in Medical Imaging: 9th International Workshop, MLMI 2018, Held in Conjunction with MICCAI 2018, Granada, Spain, September 16, 2018, Proceedings 9*, pages 55–63, Springer, 2018.
- ⁶⁶ V. Kearney, S. Haaf, A. Sudhyadhom, G. Valdes, and T. D. Solberg, An unsupervised convolutional neural network-based algorithm for deformable image registration, *Phys. Med. Biol.* **63**, 185017 (2018).
- ⁶⁷ S. Shan et al., Unsupervised end-to-end learning for deformable medical image registration, arXiv preprint arXiv:1711.08608 (2017).
- ⁶⁸ T. Sentker, F. Madesta, and R. Werner, GDL-FIRE: Deep Learning-Based Fast 4D CT Image Registration, in *International Conference on Medical Image Computing and Computer-Assisted Intervention*, pages 765–773, Springer, 2018.
- ⁶⁹ J. M. Wolterink, J. C. Zwienenberg, and C. Brune, Implicit neural representations for deformable image registration, in *International Conference on Medical Imaging with Deep Learning*, pages 1349–1359, PMLR, 2022.
- ⁷⁰ E. Dupont, H. Kim, S. Eslami, D. Rezende, and D. Rosenbaum, From data to functa: Your data point is a function and you can treat it like one, arXiv preprint arXiv:2201.12204 (2022).
- ⁷¹ M. Sezgin and B. Sankur, Survey over image thresholding techniques and quantitative performance evaluation, *Journal of Electronic imaging* **13**, 146–168 (2004).
- ⁷² X. Li, R. Bellotti, G. Meier, B. Bachtary, D. Weber, A. Lomax, J. Buhmann, and Y. Zhang, Uncertainty-aware MR-based CT synthesis for robust proton therapy planning of brain tumour, *Radiotherapy and Oncology* , 110056 (2023).
- ⁷³ R. Bellotti, J. Willmann, A. J. Lomax, A. Adelman, D. C. Weber, and J. Hrbacek, JulianA: An automatic treatment planning platform for intensity-modulated proton therapy, arXiv preprint arXiv:2305.10211 (2023).
-

-
- ⁷⁴ L. Kong et al., Breaking the dilemma of medical image-to-image translation, *Advances in Neural Information Processing Systems* **34**, 1964–1978 (2021).
- ⁷⁵ A. Thummerer, E. van der Bijl, A. Galapon Jr, J. J. Verhoeff, J. A. Langendijk, S. Both, C. N. A. van den Berg, and M. Maspero, SynthRAD2023 Grand Challenge dataset: Generating synthetic CT for radiotherapy, *Med. Phys.* (2023).
-